Fachtagung "Experimentelle Strömungsmechanik"
5. – 7. September 2017, Karlsruhe

Über die räumliche Verteilung von Druckwellen lasergenerierter Einzelblasenkavitation

On the spatial distribution of pressure waves emanating from laser induced single bubble cavitation

S. Kordel, J. Hussong
AG Lasermesstechnik der Mehrphasenströmungen
Lehrstuhl für Hydraulische Strömungsmaschinen,
Ruhr-Universität Bochum, Universitätsstr. 150, 44801 Bochum

Differential Interferometrie, Shadowgraphie, Kavitation, Druckverteilung
Differential Interferometry, Shadowgraphy, Cavitation, pressure distribution

Abstract

In the present study a combination of Shadowgraphy and Differential Interferometry is used to investigate the spatial distribution of pressure waves emanating from laser induced single bubble cavitation. The technique is successfully applied to a cavitation bubble of approximately R_{max} = 439 - 527 µm. To benchmark the accuracy of the evaluation process synthetic interference images are evaluated. From these, the curvature and peak pressure could be determined to 94% accuracy.

1 Introduction

Emitted shock waves and liquid jets after cavitation bubble implosion are the key mechanisms of cavitation induced surface damage. Collapse times and pressure amplitudes strongly depend on the cavitation bubble dynamics (Vogel et al. 1989). Most commonly, these pressure amplitudes are either measured locally with hydrophones (Vogel et al.1996) or they are extracted from the shock front velocity based on the momentum conservation (Nagayama et al. 2002). Studies to access pressure amplitudes of cavitation shock waves by means of Mach-Zehnder Interferometry have been performed by Kim et al. (2003), Alloncle et al. (1995), Ward and Emmony (1991) and Veysset et al. (2016). However, their motivation was to extract 1D pressure profiles from the interference measurements. Ward and Emmony (1990) showed that pressure profiles of pressure waves emanating from cavitation bubbles in free space assume a skewed sinusoidal shape with slowly decreasing pressure at the rear side of the pressure peak (see Fig. 5) .The focus of the present work is to study the dissipation and propagation dynamics of pressure waves at fluid-fluid and fluid-solid interfaces. For this, 2D techniques are required to gain a complete picture of the pressure and velocity field as well as the bubble dynamics.

Differential Interferometry and Shadowgraphy are combined in the present study to capture both, the cavitation bubble dynamics and corresponding instantaneous 2D pressure and pressure gradient field distribution after bubble implosion.

2 Experimental Set-up

The experimental set-up is shown in Fig. 1. A single laser pulse (laser 1) of a frequency doubled Nd:YAG laser (EverGreen 70, Quantel) is focused by an infinity corrected 20x microscope lens (CFI60, Nikon) in a water filled cuvette (test section) to generate plasma for laser induced cavitation bubbles. The laser energy is adjusted externally by rotating a λ/2 plate with respect to a polarizing beam splitter. Excess energy is collected in a beam dump.

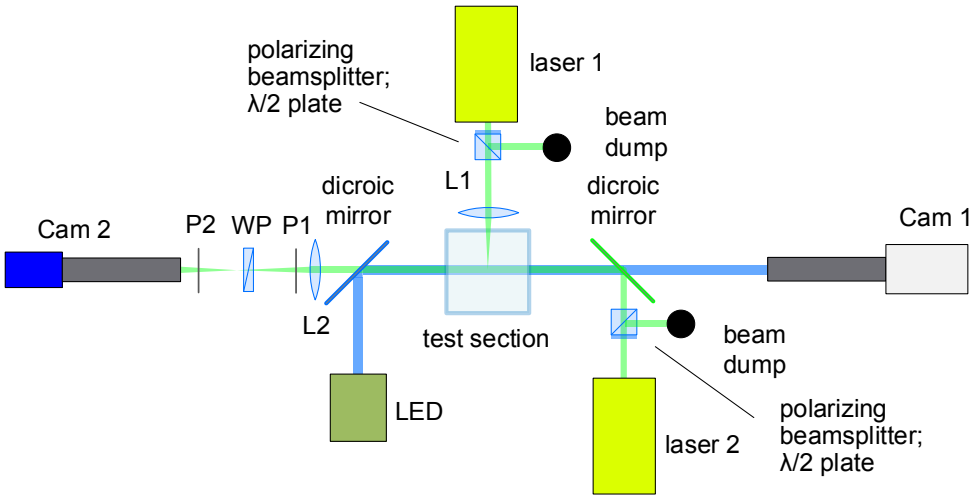

Fig. 1: Schematic of experimental set-up with combined Differential Interferometry and Shadowgraphy for pressure field measurements and bubble shadowgraphy imaging.

Bubble growth is recorded with a shadowgraphy imaging system at 77,000 fps. For this, a high-speed camera (Cam 1, Phantom Miro 110, Vision Research) with far-field microscope is focused on the expected center location of cavitation bubble nucleus. For background illumination a pulsed blue LED with a pulse width of 200 ns is synchronized with the recording sequence. The bubble evolution until collapse can be resolved with approximately 8 frames. Generated bubbles assume a maximum radius of approximately $R_{MAX} \approx 483 \pm 44$ µm.
Pressure variations in the surrounding liquid are measured with a Differential Interferometry set-up, which has been established and tested by Kordel et al. (2016). For this, a coherent light ray bundle of a second Nd:YAG laser (Litron, NanoS65) passes the test section in opposite direction to the LED light path. Again, the laser energy can be adjusted by a combination of λ/2 plate and polarizing beamsplitter. The laser beam is focused behind the test section and passes a group of polarizing filters (P1, P2) and a Wollaston Prism (W1). Interference images are recorded with a CCD camera (Cam 2, Imager ProSX, LaVision). Pressure gradient fields are deducted from phase shifts of the laser light passing through the test section.

3 Pressure Field Reconstruction

For the determination of density gradient fields, phase shifts originating from refractive index gradients of two neighboring light rays passing the measurement section of depth b with a distance d are evaluated (Merzkirch 1987). Phase differences appear as fringe shifts in the interferogram. According to (1) density gradients perpendicular to the fringe orientation $\partial\rho/\partial\zeta$ is proportional to the relative fringe displacement $\Delta S/S$. The wavelength λ and the Gladstone Dale constant K are characteristic quantities of the set-up and the chosen fluid, respectively.

$$\frac{\partial \rho}{\partial \zeta} = \frac{\lambda}{Kbd}\frac{\Delta S(x,y)}{S} \tag{1}$$

Noting that a radially propagating pressure wave in free space forms a spherical shell of finite thickness sw, the actual density gradient in radial direction $\partial\rho/\partial r$ can be deducted from the projected density gradient $\partial\rho/\partial\zeta$. For this, fringe displacements are evaluated around the pressure wave center point in azimuthal direction. To detect local fringe maxima and minima a Gaussian fitting function is used. The fringe shift is determined with an in-house Matlab code. Hence, taking into account the fringe pattern of prior recorded reference images the relative fringe displacement $\Delta S(x,y)/S$ can be determined. It may be noted that the error of relative fringe displacements gets large for small angles β between the radial coordinate direction and the fringe orientation. This is due to very small displacement values $\Delta S(x,y)/S$ as can be seen in Fig. 4 a) and b). Therefore, the present evaluation is limited to angles larger than $\beta > 15°$. To derive a continuously differentiable fringe displacement fields a linear 2D interpolation was done.

The aspect ratio of signal width sw, that is the width of the actual pressure wave signal and the ray distance d, plays a key role for the reconstruction of measured pressure waves based on (1). This influence has been investigated by means of synthetic data assuming a simple sinusoidal pressure wave function as first estimate.

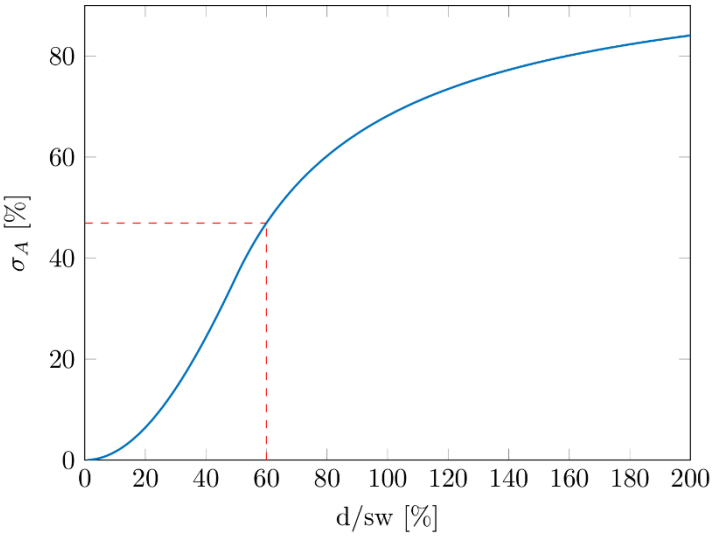

Fig. 2: Evolution of amplitude deviation as function of ray spacing d and signal width sw ratio for a sinusoidal test function

Fig. 2 shows the evolution of the amplitude deviation of a sinusoidal test signal compared to the actual signal amplitude for increasing ratios of d/sw. In the present measurements d/sw

Karlsruhe, Germany, ISBN 978-3-9816764-3-3

assumes approximately 60%. Thus, pressure amplitudes would be underestimated by approximately 47% without compensation. However, as d is a known quantity of the set-up configuration an sw may be directly extracted from recorded fringe images and therefore density gradient fields can be easily corrected for this error.
As the propagating pressure wave assumes a spherical shape, the integration depth b along the optical path is a function of radial position (see (2)):

$$b(r) = 2 \cdot \sqrt{R_{max}^2 - r^2} \tag{2}$$

Finally, as the determined density gradient field is a projection of the real radial gradient field, it is reconstructed with an inverse Abel transformation (Pretzler 1991). Assuming constant temperature, the pressure distribution can be computed using IAPWS tables.

4 Results

Cavitation bubble dynamics

Fig. 3 a) shows shadowgraphic images of the temporal evolution of a laser induced cavitation bubble. As the recording rate of the high speed camera was limited to 77 kHz the time delay between every image equals Δt = 12.99 µs. The radius of each phase was extracted and is shown in Fig. 3 b) as function of time. A maximum radius of R_{max} = 438 µm results from a sixth order polynomial fit that was applied to the data points of the first bubble cycle. The red dashed line indicates the instant at which the interference image was recorded.

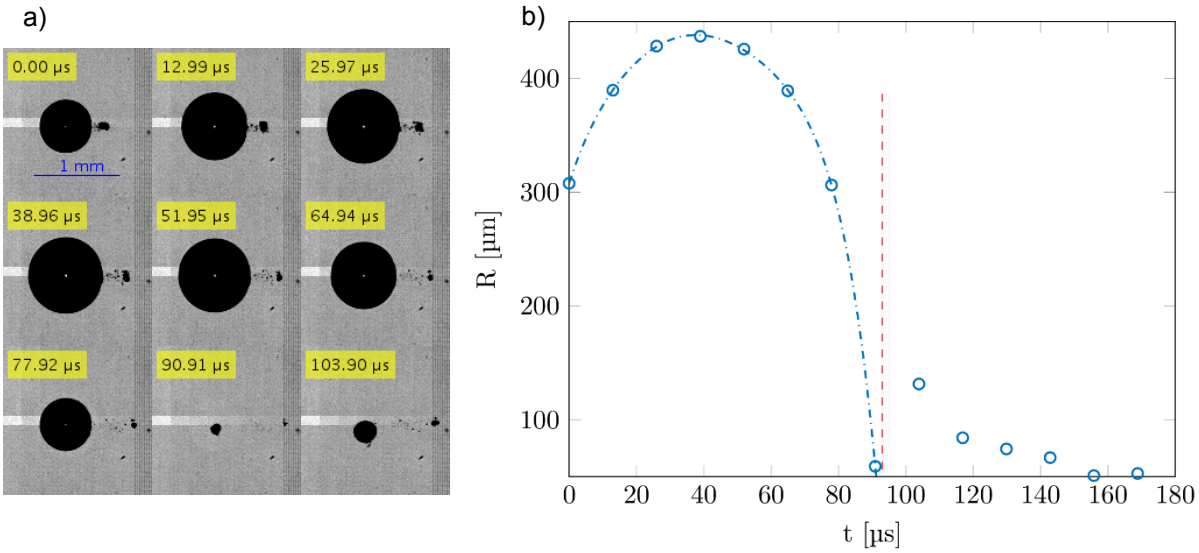

Fig. 3: a) Shadowgraphic images of the temporal evolution of a cavitation bubble at fps = 77,000; b) Temporal evolution of bubble radius; red dashed line indicates the instant at which the interference image is taken.

Reconstruction accuracy of pressure waves

In analogy to experimental measurements (see Fig. 4 a)) synthetic interferograms have been analyzed to validate the accuracy of the evaluation procedure for pressure field reconstructions. Fig. 4 b) shows a fringe pattern resulting from a synthetic pressure wave with a peak pressure of 20 bar and an inner sphere pressure of 2 bar (see Fig. 5 blue dashed line). The pressure profile is adapted from measurements of Ward & Emmony (1990).

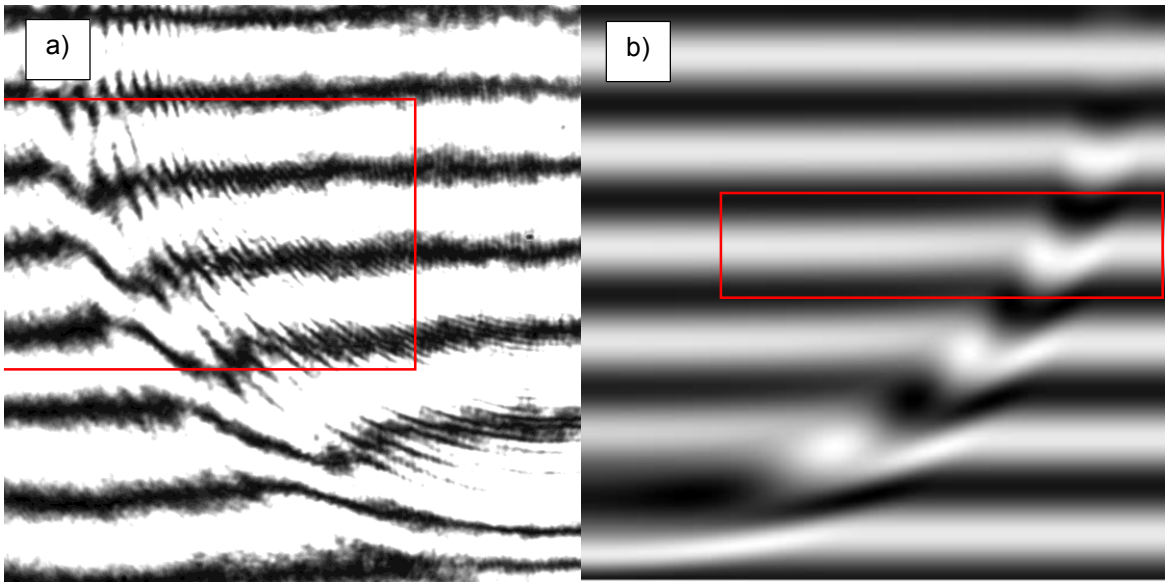

Fig. 4: a) Recorded interferogram of a pressure wave after cavitation bubble implosion; red box indicates the region of interest where fringes are evaluated; b) Synthetic interferogram assuming a peak pressure of 20 bar; red box indicates region of interest depicted for fringe evaluation.

A comparison of recorded (Fig. 4 a)) and these synthetic (Fig. 4 b)) fringe images (Fig. 4 b)), reveals very similar fringe pattern. However, in the experiments pressure waves behind the primary wave seem to induce high frequency fringe shifts, which are not present in the synthetic image data.

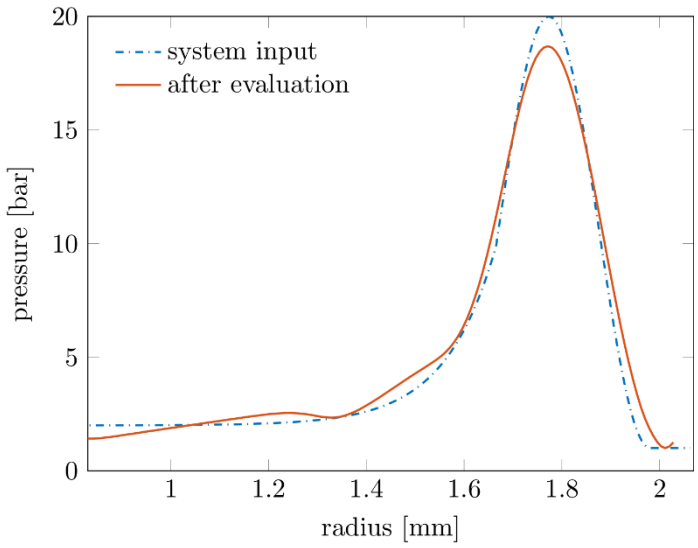

Fig. 5: Synthetically generated pressure profile (blue dashed line) and reconstructed pressure profile after evaluation (red line); The amplitude deviation equals $\sigma_A \approx 6\%$

From the synthetic image, a single fringe has been depicted (red box in Fig. 4 b)) and evaluated along radial direction. The resulting pressure profile after image evaluation is shown in Fig. 5 (red curve). The reconstruction procedure includes a median filter and a spline fitting that is applied to the pressure gradient profile before Abel inversion. This is done to achieve a robust evaluation algorithm as the Abel inversion appears to be sensitive to discontinuous curve data. Hence, the profile is numerically integrated in radial direction to recover the actual pressure profile. In a last step, a shift compensation is applied to take into account that the distance between interfering light rays induces a displacement of the actual pressure peak location. As the fringe image of Fig. 4 b) itself was created from a synthetic pressure distribution (blue dashed curve in Fig. 5), a perfect reconstruction procedure should result in identical pressure profiles. However, a small deviation in peak pressure of $\sigma_A \approx 6\%$ can be observed. Furthermore, the original curvature in the rear of the pressure wave is not fully recovered. Deviations originate predominantly from the low pass filtering and spline fitting step that is done to achieve a reconstruction algorithm that is robust against noise-influenced image data.

Pressure waves emanating from cavitation bubbles

Fig. 6 shows a depth-integrated radial density gradient field deducted from the image section shown in Fig. 4 a). A density gradient profile is extracted along the red dashed line and transformed by an Abel inversion into a radial density gradient profile (see Fig. 7). The gradient curve switches twice its sign from negative to positive values and vice versa at locations indicated by vertical red dashed lines.

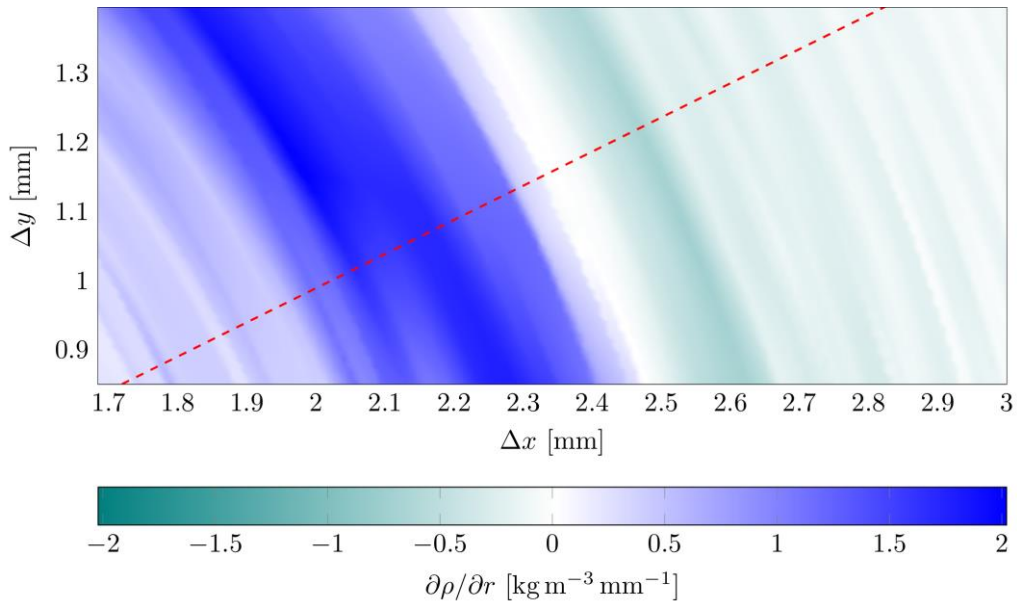

Fig. 6: Density gradient field of pressure wave after collapse of laser induced cavitation bubble; dashed line: path of extracted 1D density gradient profile

The pressure wave profile propagating in positive radial direction (red curve in Fig. 7) was deducted from the gradient field (blue dashed curve in Fig. 7). It is characterized by a pressure minimum followed by a sharp pressure increase with a peak pressure of $p_A \approx 14.1$ bar. Even though not shown here, pressure values at the rear of the primary wave may assume values above ambient pressure as the propagation distance is ($R \approx 2.27$ mm) still small (Ward & Emmony 1990). It may be noted, that in Fig. 7 details of multiple superposing pressure waves

are clearly visible in the density gradient field (blue dashed curve) while only characteristics of the primary pressure wave become visible in the pressure curve itself.

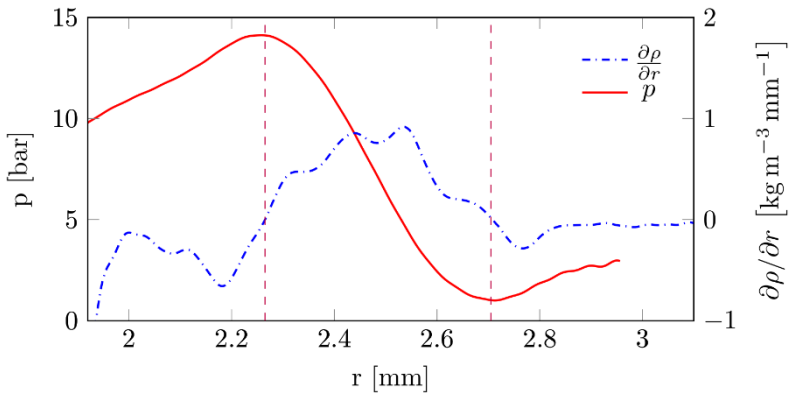

Fig. 7: Abel inversed experimental density gradient curve (blue dashed line) and corresponding pressure profile (red line) deducted from Fig. 6 (red dashed curve).

Conclusion and Outlook

In the present study density gradient fields and radial pressure distributions of a cavitation induced pressure wave have been successfully deducted from differential interferometry recordings. While in preceding works only one dimensional pressure profiles were deducted from fringe images, it is shown here that also two-dimensional gradient fields of single pressure wave events may be derived. This offers the opportunity to study more complex wave dynamics i.e. at reflecting interfaces. The present set-up allows studying cavitation bubble and pressure dynamics of the same collapse event. This is essential for estimates of kinetic energy of the pressure wave and cavitation bubble as discussed by Vogel et al. (1996). Due to a high spatial resolution (1.79 µm/pixel) details of the radial density gradient field are revealed which may not be directly accessible from pressure fields derived through Mach-Zehnder Interferometry.
Synthetic fringe images were used to evaluate the reconstruction accuracy of spherical pressure waves. Peak pressure values were deducted to 94% accuracy. The image evaluation procedure accounts for ray spacing effects that become evident when they are of comparable order compared to the pressure wave signal width sw, that is d/sw = O(1). Furthermore, a varying integral depth along the optical path for rays travelling through a spherical pressure wave of finite thickness was considered. In the present study laser-induced cavitation bubbles of $R_{max} \approx 483\pm44$ µm were investigated. A peak pressure of $p_A \approx 14.1$ bar was measured for $R_{max} = 438$µm. Currently, interferometry measurements and hydrophone recordings are combined for a direct comparison of pressure amplitude values.
In the future, refraction effects will be considered in the evaluation procedure through simultaneous interferometry measurements and speckle imaging combined with synthetic image data analysis.

Acknowledgement

This research was financially supported by DFG (HU 2264/1-1).

Literature

Alloncle, A. P., Dufresne, D., and Autric, M., 1995: “Characterization of Pressure Waves in Liquids Using an Interferometric Method.” In Shock Waves@ Marseille III (pp. 239-244). Springer Berlin Heidelberg.

Iben, U., Morozov, A., Winkelhofer, E. and Wolf, F., 2010: „Laser-pulse interferometry applied to high-pressure fluid flow in micro channels.“ Experiments in Fluids 50(3): 597–611.

Kim, B., Komashko, A., Rubenchik, A., Feit, M., Reidt, S., Da Silva, L., Eichler, J., 2003: „Interferometric Analysis of Ultrashort Pulse Laser-Induced Pressure Waves in Water.” Journal of Applied Physics 94(1): 709–715.

Kordel, S., Nowak, T., Skoda, R. and Hussong J., 2016: “Combined density gradient and velocity field measurements in transient flows by means of Differential Interferometry and Long-range µPIV.” Experiments in Fluids 57(9).

Merzkirch, W., 1987: “Flow Visualization. 2. ed.” Orlando: Acad. Press.

Nagayama, K., Mori, Y., Shimada, K. and Nakahara, M., 2002: “Shock Hugoniot Compression Curve for Water up to 1 GPa by Using a Compressed Gas Gun.” Journal of Applied Physics 91(1): 476.

Pretzler, G., 1991: “A new Method for Numerical Abel-Inversion” Z. Naturforsch. 46a, 639-641

Veysset, D., Maznev, A., Perzeril, T., Kooi, S. and Nelson, K., 2016: “Interferometric analysis of laser-driven cylindrivally focusing shock waves in a thin liquid layer” Scientific Reports, 6(1), 24.

Vogel, A., Busch, S., Parlitz, U.,1996: “Shock Wave Emission and Cavitation Bubble Generation by Picosecond and Nanosecond Optical Breakdown in Water.” The Journal of the Acoustical Society of America 100(1): 148.

Vogel, A., Lauterborn, W., and Timm, R., 1989: “Optical and Acoustic Investigations of the Dynamics of Laser-Produced Cavitation Bubbles near a Solid Boundary.” Journal of Fluid Mechanics 206(1): 299.

Ward, B., & Emmony, D. C., 1990: “The energies and pressures of acoustic transients associated with optical cavitation in water” Journal of Modern Optics 34(4): 803-811.

Ward, B., & Emmony, D. C., 1991: “Interferometric studies of the pressures developed in a liquid during infrared laser-induced cavitation-bubble oscillation.” Infrared physics, 32, 489-515.